ARTICLE

Phase transition with in-situ exsolution nanoparticles in reduced $Pr_{0.5}Ba_{0.5}Fe_{0.8}Ni_{0.2}O_{3-\delta}$ electrode for symmetric solid oxide cells

Received 00th January 20xx,
Accepted 00th January 20xx

DOI: 10.1039/x0xx00000x

Yunfeng Tian [a, b], Caichen Yang [c], Yuhao Wang [a], Min Xu [d], Yihan Ling [b], Jian Pu [c], Francesco Ciucci [a, e, f, g, h*], John T.S. Irvine [d], Bo Chi [c*]

Symmetric solid oxide cells (SSOCs) have attracted enormous attention in research and development because of their simple cell configuration and low fabrication costs. However, their development is limited by their electrocatalytic activity and stability of the electrode materials used. Herein, we report a novel perovskite oxide electrode $Pr_{0.5}Ba_{0.5}Fe_{0.8}Ni_{0.2}O_{3-\delta}$ (PBFN) approach as a highly effective SSOCs electrode material. The results demonstrate that PBFN has an outstanding electrocatalytic potential for oxygen reduction reaction, oxygen evolution reaction, carbon dioxide reduction reaction, and hydrogen oxidation reaction. After H_2 treatment, its structure changes from single to double perovskite and is accompanied by Fe-Ni alloy nanoparticle exsolution. Compared with PBFN, the SSOCs with reduced PBFN qualities show improved electrochemical performance. A reduced PBFN-based device has a higher power density (0.201 W cm^{-2} *vs.* 0.151 W cm^{-2} for H_2 as a fuel at 750 °C) and an electrolysis current density (0.524 A cm^{-2} *vs.* 0.353 A cm^{-2} for the electrolysis of pure CO_2 at 750 °C@ 2 V) in comparison to the PBFN approach as is the case with other symmetric cell results. Thus, the reduced PBFN-based device shows a favorable stability for both power density and electrolysis modes. These results suggest that phase transition and nanoparticle exsolution is a promising strategy for high performance SSOCs.

1. Introduction

Extensive use of fossil fuels has been shown increase atmospheric CO_2 concentrations, that cause enhanced climate change through accelerated global warming[1]. Moreover, solid oxide cells (SOCs) technology has shown promise as clean and efficient energy conversion and CO_2 utilization approach[2]. In fact, highly efficient SOCs can work either in fuel cell mode as SOFCs (solid oxide fuel cells) or in electrolysis cells mode as SOECs (solid oxide electrolysis cells). SOFCs can convert the chemical energy of a variety of fuels into clean electricity with high thermodynamic efficiencies[3,4], while SOECs operate in reverse, splitting water or carbon dioxide to produce H_2, CO and O_2 [5, 6]. Due to their varying environments and the required functions of the cathode and anode, conventional SOFC/SOEC often use different materials as electrodes (for example, Ni-based composites for anodes and perovskites for cathodes). Consequently, this has led to problems of material and fabrication costs, and the risk of chemical and thermomechanical incompatibility at the electrode-electrolyte interface. Moreover, the cell cannot be freely switched between SOFC and SOEC modes due to their different catalytic reactivities of the two electrodes for multiple reactions.

Symmetric solid oxide cells (SSOCs) can, however, be realized when the cathode and anode are composed of the same material[7-9]. Thus, due to the simplified configuration, material and fabrication costs can be significantly reduced[10]. Besides, in this case there is only one type of electrode-electrolyte interface, minimizing the risk of chemical and thermomechanical interfacial incompatibility[11]. Moreover, sulfur poisoning and carbon deposition can be easily removed through gas conversion when the reducing and oxidizing atmospheres are interchanged. Therefore, these devices can be used to rapidly switch between SOFC and SOEC modes[12]. Because of this enormous potential, SSOCs have captured an increasing interest in research and development. As electrodes need to be electrochemically active towards several reactions. These include the oxygen reduction reaction (ORR), oxygen evolution reaction (OER), carbon dioxide reduction reaction (CO_2RR), and hydrogen oxidation reaction (HOR), making their design particularly challenging. Therefore the development of highly active materials is crucial for the progress of SSOCs.

[a] *Department of Mechanical and Aerospace Engineering, The Hong Kong University of Science and Technology, Clear Water Bay, Hong Kong SAR, China.*
**Corresponding author E-mail: francesco.ciucci@ust.hk*
[b] *School of Materials Science and Physics, China University of Mining and Technology, Xuzhou 221116, China.*
[c] *Center for Fuel Cell Innovation, School of Materials Science and Engineering, Huazhong University of Science and Technology, Wuhan 430074, China.*
**Corresponding author E-mail: chibo@hust.edu.cn*
[d] *School of Chemistry, University of St Andrews, St Andrews, Fife, KY16 9ST Scotland, UK.*
[e] *Department of Chemical and Biological Engineering, The Hong Kong University of Science and Technology, Clear Water Bay, Hong Kong SAR, China*
[f] *HKUST Shenzhen-Hong Kong Collaborative Innovation Research Institute, Shenzhen, China.*
[g] *HKUST Energy Institute, The Hong Kong University of Science and Technology, Hong Kong SAR, China.*
[h] *Guangzhou HKUST Fok Ying Tung Research Institute, Nansha, Guangzhou 511458, China.*

† Electronic Supplementary Information (ESI) available: [details of any supplementary information available should be included here]. See DOI: 10.1039/x0xx00000x

Ti-[13,14], Cr-[11,15], Mn-[16,17], Fe-[18,19], and Co-based[20,21] perovskite oxides have been studied as electrocatalysts for SSOCs. Due to the stable electronic configuration ($3d^5$) of Fe^{3+} and the mixed-valence state of Fe [22], Fe-based perovskites are more durable than Co- and Mn-based perovskites, and also have better electrocatalytic activity than Ti- and Cr-based perovskites. In addition, Fe-based perovskites are characterized by good chemical and thermomechanical compatibility with yttria-stabilized zirconia (YSZ) or gadolinia doped-ceria (GDC)[23,24]. However, the electrochemical performance of SSOCs with the Fe-based perovskite electrodes are inferior to traditional SOFC/SOEC due to their lower conductivity and insufficient electrocatalytic activity. Therefore, there is an urgent need to enhance the electrocatalytic activity of Fe-based perovskite electrodes.

In situ exsolution of nanoparticles on the surface of perovskite oxides has generated considerable research attention in designing high performance electrode materials [25-27]. At the time of writing, the research on *in situ* exsolution mainly involving the following two categories, the matrix stable exsolution and the matrix phase transition exsolution[28]. The former are mainly suitable for Ti- and Cr-based perovskite materials [29]. Despite the positive impact of nanoparticles, their electrocatalytic activity remains low. Phase transition exsolution is an effective method to enhance the electrocatalytic activity of electrodes[30]. Kim *et al.*, found that the phase transition of $Pr_{0.5}Ba_{0.5}MnO_3$ to layered $PrBaMn_2O_{5+\delta}$ occurred under a reducing atmosphere[31]. Whereas Yu *et al.*, used Fe-doped $Pr_{0.5}Ba_{0.5}MnO_{3-\delta}$ (PBMF) as a cathode for SOEC to electrolyze CO_2 [32]. This study indicated that after the reduction of PBMF material, the perovskite structure underwent a phase transition from single to double perovskite with many Fe/MnO nanoparticles being exsolved, significantly improving the performance of CO_2 electrolysis. Liu *et al.*, developed an anode material, $Pr_{0.4}Sr_{0.6}Co_{0.2}Fe_{0.7}Nb_{0.1}O_{3-\delta}$, with *in situ* exsolved Co-Fe alloy nanoparticles accompanying the phase transition from single perovskite to R-P structure. This material achieved a remarkable electrochemical performance for direct hydrocarbon solid oxide fuel cells[33]. However, *in situ* exsolution accompanying the phase transition of Fe-based materials from single to double perovskite materials has not yet been reported. The phase transition process and the improvement of phase transition on electrocatalytic performance are yet to be explored, especially as an electrode of SSOCs.

$Pr_{0.5}Ba_{0.5}FeO_{3-\delta}$ (PBF) has been used as the cathode material of SOFC, and has achieved a high electrochemical performance[34]. This work has developed $Pr_{0.5}Ba_{0.5}Fe_{0.8}Ni_{0.2}O_{3-\delta}$ (PBFN) as a highly active SSOC electrode material, that can achieve a high electrochemical performance. Experiments had shown that the electrocatalytic activity was enhanced by the exsolution of Ni-Fe alloy nanoparticles and the concomitant phase transition from the single cubic ($Pr_{0.5}Ba_{0.5}FeO_{3-\delta}$) to A-site ordered double perovskite ($PrBaFe_2O_{5+\delta}$), which could increase the concentration of oxygen vacancies and the reactive sites. Moreover, the electrocatalytic activity of PBFN in air, CO_2, and H_2, as well as the electrochemical performance in SOFC and SOEC mode, will be discussed in detail in the sections below, alongside their demonstrated stability and redox of the corresponding SSOC devices.

2. Experimentation

2.1 Sample and cell preparation

The sol-gel method was utilized for preparing the required $Pr_{0.5}Ba_{0.5}Fe_{0.8}Ni_{0.2}O_{3-\delta}$ (PBFN) powders. $Pr(NO_3)_3{\cdot}6H_2O$, $Ba(NO_3)_2$, $Fe(NO_3)_3{\cdot}9H_2O$, and $Ni(NO_3)_2{\cdot}6H_2O$ were first dissolved in distilled water. Citric acid and ethylenediaminetetraacetic acid were then added as complexing agents. $NH_3{\cdot}H_2O$ was then added to the solution to adjust the pH to 7. The precursor gel was obtained by drying the mixture for 10 hours (h) at 80°C. The resulting PBFN powders were then obtained by additional drying (at 200°C for 5h) and annealing (1100°C in air for 5h). Next, PBFN was treated in $5\%H_2/N_2$ at 800°C for 5h; the resulting material was named R-PBFN. YSZ support (300 µm) and GDC (Ningbo SOFCMAN) was used as the electrolyte and buffer layer, respectively. PBFN/GDC/YSZ/GDC/PBFN symmetric cells were then fabricated using previously described methods [35, 36].

2.2 Characterization and measurements

X-ray diffraction (Cu Kα, 40 kV, 30 mA, scanning stepping of 0.05°, Shimadzu XRD-7000S) was used to characterize the crystal structure of PBFN and R-PBFN. To document the electrode microstructure, field emission scanning electron microscopy (FSEM, Carl Zeiss GeminiSEM300) and energy dispersive spectroscopy (EDS) were used. Further to this, transmission electron microscopy (TEM), EDS analysis, and electron energy loss spectroscopy (EELS) analysis were conducted using an FEI Titan Themis instrument. To demonstrate the phase transition process, the thermogravimetric (TG) curve of pre-dried powders was recorded by TGA (STA449F5, NETZSCH) in $5\%H_2/N_2$ with a heating rate of 10 °C·min^{-1}. Then, the hydrogen temperature-programmed reduction (H_2-TPR) test was also carried out using a piece of homemade equipment, that included a mass spectrometer and a furnace. The samples were first put in a U-type quartz tube and kept in Ar at 350 °C for 1 h, and then heated to 950°C in 5% H_2/N_2. X-ray photoelectron spectroscopy (XPS, VG Multilab 2000) was subsequently conducted to estimate the oxidation state of Fe, Ni, O on the surfaces of the samples. Electron spin resonance (ESR) measurements were carried out on a JEOL JES-FA200 to prove oxygen vacancy concentration.

PBFN/GDC/YSZ/GDC/PBFN symmetric cells were used first to measure the polarization resistance (R_p) of the PBFN electrode in air, CO_2, and H_2. For full cell performance testing, the cell was sealed in Al_2O_3 tubes with a ceramic adhesive (552-VFG, Aremco). During fuel cell tests, one side of the cell was fed with 50 mL·min^{-1} of H_2 and the other with 50 mL·min^{-1} of air. For the SOEC tests, one side of the cell was fed with 50 mL·min^{-1} of CO_2 and the other with 50 mL·min^{-1} of air. To complete the phase transition and exsolution process, the PBFN was treated

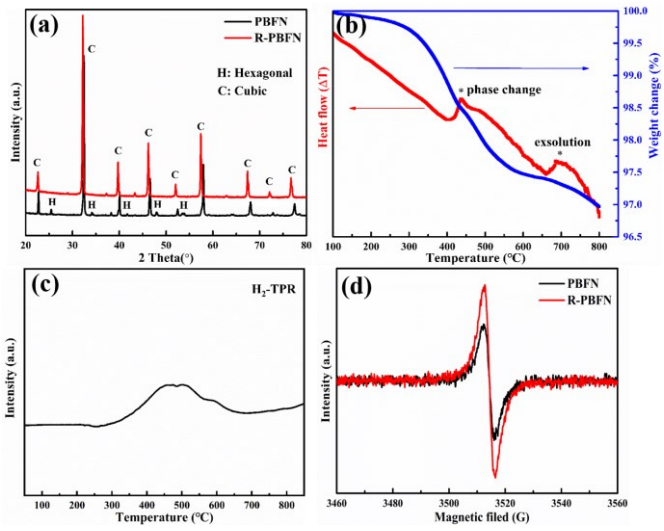

Fig. 1 (a) XRD patterns of PBFN and R-PBFN, (b) TG curves of PBFN in 5%H_2/N_2, (c) H_2-TPR curves of PBFN, and (d) ESR curves of PBFN and R-PBFN.

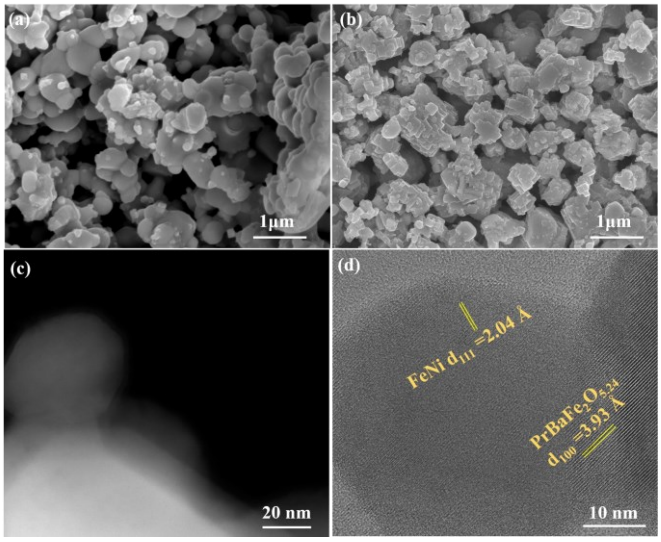

Fig. 2 SEM images of (a) PBFN and (b) R-PBFN; (c) TEM and (d) HRTEM of R-PBFN.

in 5%H_2/N_2 at 800°C for 5h. The cell structure changed into R-PBFN/GDC/YSZ/GDC/PBFN. The electrochemical impedance spectra (EIS) were recorded by an electrochemical workstation (Zennium IM6 station) in the frequency range from 0.1 to 10^5 Hz with an amplitude of 20 mV. Polarization curves were tested with a linear sweep rate of 0.01 V/s from 0 V to the open-circuit voltage (OCV) for fuel cell operation and from 0 to 2.0 V for SOEC. The 60h stability test in fuel cell and the CO_2 electrolysis mode was performed.

3. Results and discussion

3.1 Phase analysis and chemical stability

XRD patterns of the PBFN and R-PBFN powders are presented in Figure 1(a). The pattern for the PBFN sample indicated a mixture of cubic (C) and hexagonal (H) phases. After reducing in 5%H_2/N_2 for 5h at 800°C, the hexagonal (H) phase could no longer be detected, which is consistent with a phase transition of R-PBFN from $Pr_{0.5}Ba_{0.5}FeO_{3-\delta}$ to $PrBaFe_2O_{5+\delta}$ and similar to the PBM literature[31,37]. Furthermore, the XRD pattern of R-PBFN had a diffraction peak at 44° corresponding to Fe-Ni alloy and, therefore, confirming the exsolution of Fe-Ni alloy nanoparticles. Calculated particle size of nanoparticles was 35.6 nm according to the Scherrer equation. The exsolution and phase transition was further probed by the thermogravimetric analysis (see Figure 1(b)), which suggests that oxygen loss and exsolution mainly consists of three stages. The first stage was the desorption of adsorbed water before 300 °C, and the second stage from 300 to 600°C could be attributed to oxygen loss and phase transition. In fact, a sharp exothermic peak (*) at 400°C indicates that the phase change was from single to double perovskite. The third and last stage above 600°C corresponds to the exsolution of Fe-Ni alloy nanoparticles. The oxygen loss and phase transition could then be confirmed by H_2-TPR results (see Figure 1(c)). The substantial H_2 consumption detected from 300 to 600°C could be attributed to a reduction-induced phase transition. ESR was used to demonstrate the generation of a large number of oxygen vacancies[38,39]. The relative intensity of the peak represented the degree of oxygen loss. The stronger ESR intensity also showed that oxygen vacancies were generated through reduction (Figure 1(d)). In summary, upon reduction, the structure of PBFN changed from single to double perovskite, Fe-Ni alloy nanoparticles were exsolved, and oxygen vacancies were formed. As will be illustrated later, these factors contributed to improving electrocatalytic activity.

3.2 Morphology characterization

SEM images of PBFN and R-PBFN are shown in Figure 2. above. The shape of the PBFN powders were roughly spherical with a particle diameter of around 500 nm (see Figure 2(a)). After reduction, the shape of the perovskite particles changed as shown in Figure 2(b) and Figure S1, which suggested a concomitant phase change. In addition, nanoparticles with an average particle size of 30 nm were observed in R-PBFN (see Figure 2(b) and Figure S2). The in-situ exsolved nanoparticles were further characterized by TEM (see Figure 2(c)). The characteristic spacings of 0.204 nm and 0.393 nm could be attributed to the (111) lattice planes of the Fe-Ni alloy and the (100) lattice plane of the $PrBaFe_2O_{5+\delta}$, respectively. EDS mapping images and line scanning analysis shown in Figure S3 further indicate that the exsolved nanoparticles are Fe-Ni alloy. The exsolution of Ni-Fe alloy nanoparticles and the concomitant phase transition are also in agreement with the XRD results. These results further support the hypothesis that the reduction process triggered a phase transition in PBFN and the exsolution of Fe-Ni alloy nanoparticles.

HRTEM was carried out to study the microstructural and interfacial properties of the R-PBFN. The detected spacings of 0.277 nm and 0.386 nm, which could be attributed to the (110) and the (002) lattice planes of the $PrBaFe_2O_{5+\delta}$ (see Figure 3(a) below), indicated that the crystal structure of the perovskites changed. From a more detailed HRTEM image (see Figure 3(a), two white boxes), the perovskite oxide had a distortion along the c-direction lattice, which could be caused by the single perovskite-double perovskite transition process. The *in situ*

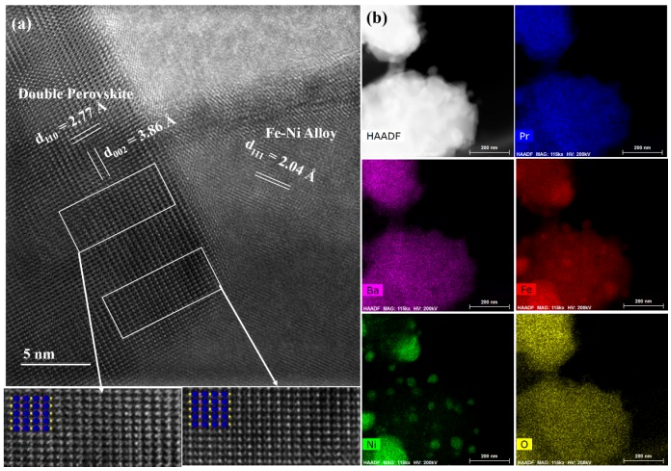

Fig. 3 HRTEM of R-PBFN (a) and the EDS mapping of R-PBFN(b).

exsolved nanoparticles showed a characteristic spacing of 0.204 nm for the (111) lattice plane of the Fe-Ni alloy. Moreover, the coherency of the interface between Fe/Ni and double perovskite matrix facilitated the improvement of electrocatalytic activity and stability, because of their tightly anchored structure and small nanoparticles. Meanwhile, the PBFN HRTEM with the corresponding EDS (see Figure S4) confirmed the uniform elemental distribution before reduction. After reduction, Ni and Fe aggregate (visible in Figure 3(b)) supported the occurrence of exsolution. The diameter of the exsolved nanoparticles was ~30 nm, which was consistent with the XRD and SEM results.

3.3 XPS characterization

XPS was used to characterize the surface element oxidation state of PBFN and R-PBFN samples and confirm the presence of exsolved Fe-Ni nanoparticles. Figure 4(a) shows the spectra of Fe 2p3/2 and Fe 2p1/2 of samples. The two peaks being centered at 709.9/723.4 eV and 712.4/726.2 eV could be assigned to Fe^{2+} and Fe^{3+}, respectively. Upon reduction the two peaks (707.5 and 720.6 eV) corresponding to metallic Fe^0 emerge[40]. For the Ni 2p spectra of the PBFN samples, peaks at 855.1 and 872.2 eV could be attributed to Ni 2p3/2 and Ni 2p1/2, respectively (see Figure 4(b)) with these features at 862 eV and 879.7 eV representing their satellite peaks. Moreover, peaks for metallic Ni were observed in the R-PBFN sample, validating the existence of metallic Ni^0 as well as the exsolution of nanoparticles in R-PBFN[41]. The exsolution of Fe-Ni alloy nanoparticles could be confirmed by HRTEM-EELS results as shown in Figure S6. As presented in Figure 4(c), the O_{1s} spectrum had three components corresponding to the hydroxyl (-OH, ~532.5 eV) from external H_2O, surface oxygen-containing species (O_S, ~531.2 eV), and the lattice oxygen (O_L,~528.3 eV)[41]. The O_S feature indicated the presence of oxygen-containing species (*e.g.*, O_2 and CO_2) at the surface. The O_S relative concentration in R-PBFN is 63.55%, which is a value 14% higher than that of PBFN (49.01%), implying an enhanced chemisorption of oxygen-containing species in R-PBFN with their corresponding improvements in CO_2RR and ORR activities.

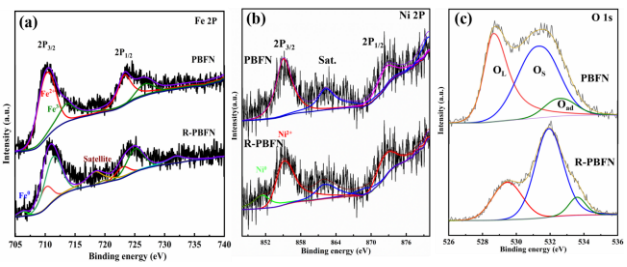

Fig. 4 XPS spectra of Fe 2p (a), Ni 2p (b) and O 1s (c) for PBFN and R-PBFN.

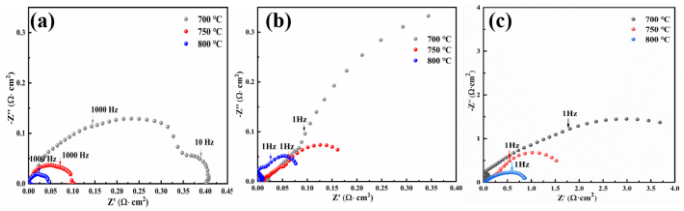

Fig. 5 EIS of pure PBFN electrode in air (a), H_2 (b), CO_2 (c) at different temperatures.

3.4 Polarization resistance of the symmetric cell

The polarization resistance, R_p, of the PBFN symmetric cell in various atmospheres and temperatures are presented in Figure 5. From 700 to 800°C, R_p values were 0.408, 0.103, and 0.047 Ω·cm² in air (see Figure 5(a)), and 3.688, 1.523, and 0.864 Ω·cm² in CO_2 (see Figure 5(c)), respectively. R_P values in CO_2 were larger than those in air, which could be attributed to the CO_2RR being weaker than the ORR of the PBFN electrode. R_p values in H_2 were also smaller (see Figure 5(b)), implying a high HOR activity. Overall, the results indicated that PBFN electrodes possess good ORR, OER, CO_2-RR, and HOR catalytic activity.

3.5 Electrochemical performance in SOFC mode

The SOFC performance is shown in Figure 6. The maximum power densities of cells were 0.071, 0.151, and 0.261 W·cm^{-2} at 700, 750, and 800°C, respectively. Relative to other symmetric electrode literature reports (see Table S1), the PBFN cell achieved promising electrochemical performance. Figure 6(b) shows the EIS curves for the cell at various temperatures. Generally, the intersection value of the high frequency of EIS along the real axis represents the ohmic resistance (R_s). The value between the intersection of the high frequency and low frequency with the real axis is R_p. Values of R_s were 1.871, 1.12, and 0.704 Ω·cm² while the values of R_p were 1.941, 0.575, and 0.306 Ω·cm² at 700, 750, 800°C, respectively. R_s can thus, be

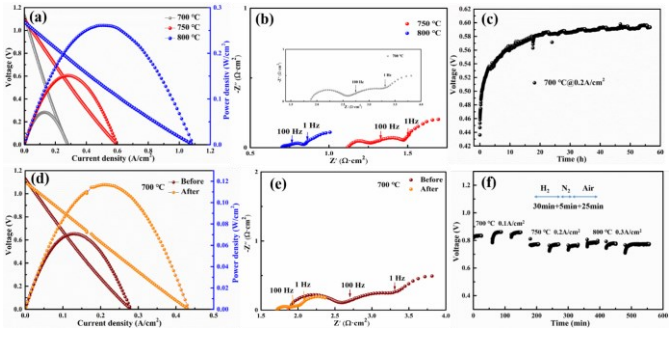

Fig. 6 SOFC performance at various temperatures I-V-P plot (a) and EIS curves (b), the short stability test in SOFC mode (c), The I-V-P curve (d) and EIS (e) PBFN before and after test, the redox stability test in SOFC mode (f).

ascribed to charge transport, including the resistance of the YSZ electrolyte (thickness of 300 μm), the contact resistance between the electrode and the YSZ, GDC barrier layer, and Pt collector. Conversely, R_p depends on charge transfer at the electrode surface kinetics, and CO_2 transport and adsorption. A pure PBFN electrode in SOFC mode of the SSOCs exhibited higher power density and a lower R_p, implying higher HOR and ORR activities. The output voltage increased from 0.44 V to 0.6 V during the discharge process as shown in Figure 6(c), which indicated SOFC performance improvement. After repeating the experiment, the results were the same with performance gradually improving as shown in Figure S7. Continuous exsolution of Fe-Ni nanoparticles in a reducing atmosphere led to an increase in electrocatalytic activity. Subsequently, the peak power density of the test cell (~ 0.12 W·cm^{-2}) was 70% higher than that of the cell before the test (~0.071 W·cm^{-2}) and after the phase change along with the Fe-Ni alloy exsolution as shown in Figure 6(d). Moreover, both the R_s and R_p were reduced, especially the R_p, which decreased from 1.941 Ω·cm^2 to 0.649 Ω·cm^2 (see Figure 6(e)). The detailed electrochemical performance of the R-PBFN cell at different temperatures is shown in Figure S8, and alongside this, Figure 6(f) shows the redox stability of the cell. Specifically, the cell first worked in SOFC mode at 0.1A·cm^{-2} for 30 min at 700°C, then was switched to N_2 for 5 min, and finally switched back to air for 25 min of oxidation treatment. Cell performance remained almost unchanged after 3 cycles. Moreover, regardless of operation at higher temperatures (750°C and 800°C) or at higher current densities (0.2 A·cm^{-2} and 0.3 A·cm^{-2}), the cell performance remained stable. These results thus indicate that a PBFN cell had a workable redox stability.

3.6 Electrochemical performance in SOEC mode

The SOEC performance for pure CO_2 electrolysis based on R-PBFN electrodes is presented in Figure 7(a). The electrolysis current density increased gradually with the raising of temperature. The corresponding values were 0.322, 0.524, and 0.843 A·cm^{-2} under 2.0 V at 700, 750, and 800 °C, respectively. This also showed an improved performance compared with other symmetric cells as listed in Table S2. The corresponding EIS is shown in Figure 7(b). R_s values were 2.313, 1.662, and 1.151 Ω·cm^2 and R_p values of were 5.285, 3.979, and 2.56 Ω·cm^2 at 700, 750 and 800°C, respectively. The EIS of the cell at the working temperature (1.4 V) is shown in Figure 7(c). The R_p was only 0.88 Ω·cm^2 at 800°C at 1.4 V. Figure 7(d) shows the I-V curves of PBFN and R-PBFN cells at 750°C for pure CO_2 electrolysis. The current density of the R-PBFN cell was 0.524 A·cm^{-2} at 2.0 V, approximately 48% higher than that of PBFN (0.353 A·cm^{-2}) at 750°C. The detailed electrochemical performance of the PBFN cell at different temperatures is presented in Figure S9 below. The EIS of two cells under OCV at 750 °C are also shown in Figure 7(f). The value of R_p with R-PBFN cell was clearly lower than that of the cell with PBFN (3.979 Ω·cm^2 vs 5.962 Ω·cm^2) at 750°C. Moreover, the R_p of R-PBFN cell was also obviously lower than that of the cell with PBFN (1.021 Ω·cm^2 vs 1.351 Ω·cm^2) in working conditions at 750°C. These results demonstrated that the R-PBFN cell had substantially increased CO_2 electrolysis performance. The specific mechanism underpinning the performance of PBFN will be studied in future research.

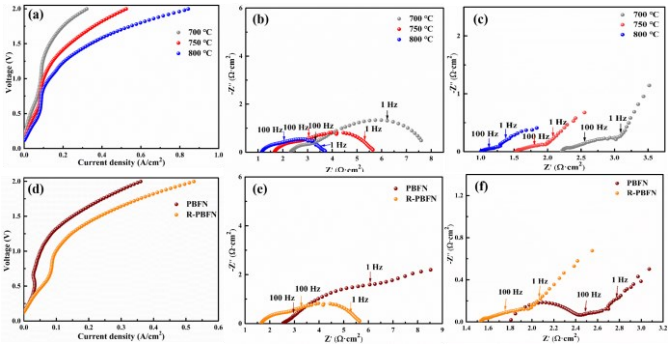

Fig. 7 I-V curves (a) and EIS of the R-PBFN based SSOC for pure CO_2 electrolysis at OCV (b) and under working conditions (1.4V) (c) at different temperatures. The performance comparison of PBFN and R-PBFN, I-V curves (d), EIS at OCV (e), and working conditions (1.4V) (f) at 750 °C.

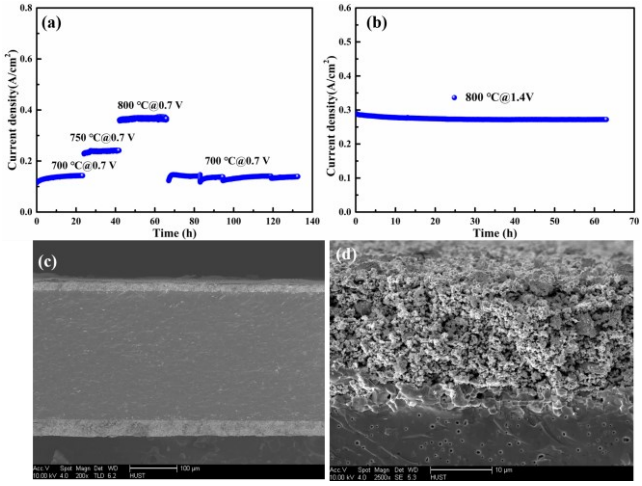

Fig. 8 The long-term stability test in SOFC mode (a) and SOEC mode (b); the

3.7 Stability of SSOCs

To evaluate the reliability of PBFN electrodes, the SSOCs were operated in SOFC mode at 700°C for ~24h, as presented in Figure 8(a), wherein the performance improved. Subsequently, the cell performed stably without any noticeable degradation at different temperatures, which demonstrated that the PBFN cells had satisfactory SOFC electrochemical stability. At this point the cell worked in SOEC mode, which was equal to the R-PBFN electrode. The current density decreased slightly for the first few hours and then stabilized as shown in Figure 8(b). In general, the current density of electrolysis was around 0.28 A·cm^{-2} under 1.4 V at 800°C for pure CO_2 electrolysis, implying good long-term stability. As shown in Figure 8(c, d), the structure was also stable with no delamination occurring.

Conclusions

This work developed a novel, highly active perovskite catalyst $Pr_{0.5}Ba_{0.5}Fe_{0.8}Ni_{0.2}O_{3-\delta}$ as electrodes of SSOC for power out and

CO_2 electrolysis. Owing to the phase transition and exsolved nanoparticles, this new electrode displayed an excellent ORR, OER, CO_2RR, and HOR performance. R_P values in air, CO_2, and H_2 are 0.108, 0.864, and 0.1 Ω·cm^2 at 800°C, respectively, which were smaller than other symmetric electrode results. Quasi-symmetric electrolyte-supported R-PBFN electrodes exhibited outstanding electrochemical performance with the maximum power density reaching 300 mW·cm^{-2} at 800°C in fuel cell mode. When operated as a CO_2 electrolyzer, the cell displayed a small polarization resistance of 0.88 Ω·cm^2 at 1.4 V and a maximum current density of 0.843 A·cm^{-2} at a voltage of 2.0 V at 800°C. Most importantly, SSOCs with quasi-symmetric R-PBFN electrodes operated robustly in both SOFC and SOEC modes. Overall, this work has demonstrated a highly promising strategy with phase transition and exsolution for producing electrodes for the next generation of SOCs.

Author contributions

Yunfeng Tian: investigation, formal analysis, writing - original draft, visualization. **Caichen Yang**: data curation. **Yuhao Wang**: data curation. **Min Xu**: data curation. **Yihan Ling**: data curation, funding acquisition. **Jian Pu**: data curation, funding acquisition. **Francesco Ciucci**: supervision, funding acquisition, writing – extensive review & editing, analysis. **John T S Irvine**: supervision, conceptualization. **Bo Chi**: project administration, funding acquisition. supervision, writing – review& editing.

Conflicts of interest

There are no conflicts to declare.

Acknowledgements

YT, YW, and FC gratefully acknowledge the Research Grant Council of Hong Kong for support through the projects 16206019 and 16201820 as well as the Hong Kong Scholar program (XJ2021048). This work was supported in part by the Project of Hetao Shenzhen-Hong Kong Science and Technology Innovation Cooperation Zone (HZQB-KCZYB-2020083). We gratefully appreciate for financial support from National Key Research & Development Project (2020YFB1506304, 2017YFE0129300), National Natural Science Foundation of China (52172199, 52072135, 52002121), Fundamental Research Funds for the Central Universities (2021QN1111), the MOE Key Laboratory for the Green Preparation and Application of Functional Materials, the Jiangsu Key Laboratory of Coal-based Greenhouse Gas Control and Utilization (2020KF04), and the Open Sharing Fund for the Large-scale Instruments and Equipment of China University of Mining and Technology (CUMT), the Analytical and Testing Centre of Huazhong University of Science and Technology are all appreciated for their sample characterizations assistance. The authors would also like to thank the Materials Characterization and Preparation Facilities (MCPF) of HKUST for their kind technical assistance.

References

1. D. Hidalgo; J. Martín-Marroquín, *Renew Sust Energ Rev.* 2020, **132**, 110057.
2. C. Ni; J. Zhou; Z. Zhang; S. Li; J.-P. Ni; K. Wu; J. Irvine, *Energy Environ. Sci.* 2021, **14**, 6287-6319.
3. M. B. Hanif; M. Motola; S. Rauf; C.-J. Li; C.-X. Li, *Chem Eng J* 2022**, 428**, 132603.
4. Y. Zhang; B. Chen; D. Guan; M. Xu; R. Ran; M. Ni; W. Zhou; R. O'Hayre; Z. Shao, *Nature* 2021**, 591** (7849), 246-251.
5. H. Shimada; T. Yamaguchi; H. Kishimoto; H. Sumi; Y. Yamaguchi; K. Nomura; Y. Fujishiro, *Nat. Commun.* 2019, **10** (1), 1-10.
6. A. Hauch; R. Küngas; P. Blennow; A. B. Hansen; J. B. Hansen; B. V. Mathiesen; M. B. Mogensen, *Science* 2020, **370** (6513).
7. D. Huan; L. Zhang; S. Zhang; N. Shi; X. Li; K. Zhu; C. Xia; R. Peng; Y. Lu, *J. Mater. Chem. A* 2021**, 9** (5), 2706-2713.
8. J. Zamudio-García; L. Caizán-Juanarena; J. M. Porras-Vázquez; E. R. Losilla; D. Marrero-López, *J. Power Sources* 2022**, 520**, 230852.
9. Y. Tian; N. Abhishek; C. Yang; R. Yang; S. Choi; B. Chi; J. Pu; Y. Ling; J. T. Irvine; G. Kim, *Matter* 2022**, 5** (2), 482-514.
10. C. Su; W. Wang; M. Liu; M. O. Tadé; Z. Shao, *Adv. Energy. Mater.* 2015**, 5** (14), 1500188.
11. J. Wang; J. Zhou; J. Yang; D. Neagu; L. Fu; Z. Lian; T. H. Shin; K. Wu, *Adv. Mater. Inter* 2020**, 7** (23), 2000828.
12. Y. Tian; Y. Liu; L. Jia; A. Naden; J. Chen; B. Chi; J. Pu; J. T. Irvine; J. Li, *J. Power Sources* 2020**, 475**, 228620.
13. C. Arrive; T. Delahaye; O. Joubert; G. H. Gauthier, *Ceram Inter* 2020**, 46** (5), 5841-5849.
14. C. Arrivé; T. Delahaye; O. Joubert; G. H. Gauthier, *Ceram Inter* 2020**, 46** (15), 23442-23456.
15. Y. Wan; Y. Xing; Z. Xu; S. Xue; S. Zhang; C. Xia, *Appl Catal B: Environ* 2020**, 269**, 118809.
16. X. Luo; Y. Yang; Y. Yang; D. Tian; X. Lu; Y. Chen; Q. Huang; B. Lin, *Electrochim. Acta* 2018**, 260**, 121-128.
17. S. Kim; G. Kim; A. Manthiram, *J. Power Sources* 2021**, 497**, 229873.
18. J. Wang; L. Fu; J. Yang; K. Wu; J. Zhou; K. Wu, *J Rare Earth* 2021, **39**(9), 1095-1099.
19. Y. Cao; Z. Zhu; Y. Zhao; W. Zhao; Z. Wei; T. Liu, *J. Power Sources* 2020**, 455**, 227951.
20. B.-K. Lai; K. Kerman; S. Ramanathan, *J. Power Sources* 2011**, 196** (4), 1826-1832.
21. N. Duan; J. Yang; M. Gao; B. Zhang; J.-L. Luo; Y. Du; M. Xu; L. Jia; B. Chi; J. Li, *Nano Energy* 2020**, 77**, 105207.
22. K. Wang; C. Han; Z. Shao; J. Qiu; S. Wang; S. Liu, *Adv. Funct. Mater.* 2021**, 31** (30), 2102089.
23. M. D. Anderson; J. W. Stevenson; S. P. Simner, *J. Power Sources* 2004**, 129** (2), 188-192.
24. G. Yang; C. Su; Y. Chen; M. O. Tade; Z. Shao, *J. Mater. Chem. A* 2014**, 2** (45), 19526-19535.
25. X. Sun; H. Chen; Y. Yin; M. T. Curnan; J. W. Han; Y. Chen; Z. Ma, *Small* 2021**, 17** (10), 2005383.
26. J. Zhang; M.-R. Gao; J.-L. Luo, *Chem. Mater* 2020**, 32** (13), 5424-5441.
27. J.-h. Myung; D. Neagu; D. N. Miller; J. T. Irvine, *Nature* 2016**, 537** (7621), 528-531.
28. J. H. Kim; J. K. Kim; J. Liu; A. Curcio; J.-S. Jang; I.-D. Kim; F. Ciucci; W. Jung, *ACS nano* 2020**, 15** (1), 81-110.

29. Y. Gao; D. Chen; M. Saccoccio; Z. Lu; F. Ciucci, *Nano Energy* 2016**, 27**, 499-508.
30. J. Wang; Y. Gao; D. Chen; J. Liu; Z. Zhang; Z. Shao; F. Ciucci, *ACS Catal* 2018**, 8** (1), 364-371.
31. S. Sengodan; S. Choi; A. Jun; T. H. Shin; Y.-W. Ju; H. Y. Jeong; J. Shin; J. T. Irvine; G. Kim, *Nat. Mater.* 2015**, 14** (2), 205-209.
32. J. Zhu; W. Zhang; Y. Li; W. Yue; G. Geng; B. Yu, *Appl Catal B: Environ* 2020**, 268**, 118389.
33. C. Yang; J. Li; Y. Lin; J. Liu; F. Chen; M. Liu, *Nano Energy* 2015**, 11**, 704-710.
34. Y. Meng; Q. Zhang; Z. Chen; X. Chen; J. Zhou; X. Zhu; N. Wang; D. Zhou, Ionics 2021, 27, 3951-3965.
35. Y. Tian; H. Zheng; L. Zhang; B. Chi; J. Pu; J. Li, *J. Electrochem. Soc* 2018**, 165** (2), F17.
36. Y. Tian; C. Yang; Y. Li; S. He; X. Wang; Y. Ling; W. Li; B. Chi; J. Pu, *J. Electrochem. Soc* 2021**, 168** (10), 104515.
37. L. Zhao; K. Chen; Y. Liu; B. He, *J. Power Sources* 2017**, 342**, 313-319.
38. L. Zou; Y. Tian; J. Pu; B. Chi, *J Alloy Compd* 2022**, 900**, 163540.
39. J. Ma; F. Zhu; Y. Pan; H. Zhang; K. Xu; Y. Wang; Y. Chen, *Sep Purif Technol* 2022, 120657.
40. K. Sun; J. Liu; J. Feng; H. Yuan; M. He; C. Xu; Z. Wang; W. Sun; J. Qiao, *J. Power Sources* 2017**, 365**, 109-116.
41. K. J. Kim; M. K. Rath; H. H. Kwak; H. J. Kim; J. W. Han; S.-T. Hong; K. T. Lee, *ACS Catal* 2019**, 9** (2), 1172-1182.